

Experimental Study on Wake Characteristics of Secondary Grooved Cylinders with Different Depths

F. Peng, F. Yan[†], B. J. Yin and J. N. Liang

School of Mechanical Engineering, Jiangsu University of Science and Technology, Jiangsu, Zhenjiang 212000, China

[†]Corresponding Author Email: yanfei@just.edu.cn

(Received October 2, 2022; accepted January 15, 2023)

ABSTRACT

In this study, the flow field of a new secondary-grooved cylinder is determined by using particle image velocimetry (PIV) to understand the wake characteristics at different depths of the secondary grooved cylinders. In order to analyze the wake characteristic behind the secondary grooved cylinder with different depths, time-averaged streamlines, time-averaged velocity, RMS velocity, Reynolds stress, turbulent kinetic energy, and instantaneous flow structures are employed. The recirculation zone for secondary grooved cylinders with different depths decreases when compared to the smooth cylinder; the peak magnitudes of flow velocity fluctuation intensity and transverse velocity fluctuation intensity for secondary grooved cylinders with different depths are reduced and the locations appear delayed. Furthermore, in contrast to the smooth cylinder, the secondary grooved cylinders with different depths' Reynolds stress and turbulent kinetic energy are increased by the wake flow, and the transient large-scale vortex is split into several smaller-scale vortices behind the secondary grooved cylinders. The results obtained for the above flow structure are more significant when $h/D = 0.05$ for the secondary grooved cylinder.

Keywords: Wake characteristic; Secondary grooved cylinder; PIV; Recirculation region; Reynolds stress.

NOMENCLATURE

D	cylinder diameter	$\overline{u'v'}/U^2$	normalized Reynolds stress in the (x, y)-plane
h	roughness height	$\overline{u'w'}/U^2$	Reynolds stress in the (x, z)-plane
L	length of the cylinder	v'	transverse velocity pulsation component
S	cross-sectional area	v_{rms}/U	transverse velocity fluctuating intensity
TKE	turbulent kinetic energy	w'	longitudinal velocity pulsation component
\bar{u}	streamwise velocity	x	flow direction
u	water velocity	y	lateral direction
u'	flow velocity pulsation component	z	longitudinal direction
u_{rms}/U	streamline velocity fluctuating intensity		
\bar{u}/U	time-averaged streamwise velocity		

1. INTRODUCTION

It Fluid flowing around cylinders is a common physical occurrence in nature and in maritime engineering projects such as tension-leg platforms, marine risers, and marine pipelines. Regardless of geometrical variations, the primary feature of the thin cylinder's wake is the creation of vortex shedding—which can result in drag force, lift fluctuation, structural vibration, and noise (Zheng

and Rinoshik 2020). In an effort to mitigate these negative consequences, many academics have modified the wake flows behind the cylinder using passive devices on its surface. In the past, the rigid splitter plate (Hwang and Yang 2007; Xie *et al.* 2015; Liu *et al.* 2016) and fairing structures (Gu *et al.* 2012; Assi *et al.* 2014) were the most successful and widely used vortex suppression devices. Fairings and a stiff splitter plate can reduce drag the most, but they are only useful in certain conditions. Passive flow

control using biomimicry on groove surfaces may be effectively decreased through technology.

Dimples (Zhou *et al.* 2015b; Wang *et al.* 2017), the fin-shaped strip (Zhu and Zhou 2019), the wavy (Xu *et al.* 2010), helical strakes (Zhou *et al.* 2011), riblets (Liu *et al.* 2009), and grooves are among the techniques being developed to reduce flow resistance around cylinders (Quintavalla *et al.* 2013; Zheng *et al.* 2021). Among these, the grooved surface can suppress vortices and minimize drag better than adding devices to the cylinder's surface (Zhou *et al.* 2015a). Huang (2011) investigated the effects of triple beginning helical grooves on the drag of stationary circular cylinders and the vortex-induced vibration of cylinders supported by elastic using an experimental approach. The results show that the helical grooves successfully suppress the cross-flow vibration amplitude caused by the vortex, and the peak amplitude is reduced by 64%. The helical grooves reduce the drag of fixed cylinders by around 25% in the sub-critical Reynolds number region Canpolat (2015) investigated the flow characteristics of a single groove on the cylinder surface using the particle image velocimetry (PIV) method. It was discovered that the size of the groove influences the frequency with which Karman vortex sheaths occur. Particle image velocimetry was utilized by Canpolat (2017) to examine the single grooves on cylindrical surfaces' ability to influence flow. Consequently, the flow properties of the cylinder wake are displayed. Qian and Wang (2019) used numerical simulations to conduct in-depth research on the smooth cylinder and grooved cylinder flow around drag and flow field features at sub-Reynolds numbers. The greatest drag reduction rate is 28.4%, and V-grooved cylinders were found to have a greater drag reduction impact than smooth cylinders. The V-groove also helps by changing the frequency of vortex shedding and the growth of turbulence in the wake zone, Afroz and Sharif (2022) performed numerical simulations of laminar cross-flow across the smooth cylinder and three different types of longitudinally grooved cylinder surfaces at low Reynolds numbers (the triangular V-shaped, the U-shaped, and the Rectangular shaped grooves). Conclusion: At Reynolds numbers of around 200 and 300, the U-groove structure reduced the mean drag coefficient by 13% and 10%, respectively, when compared to a smooth cylinder.

The special structures on the surface of many organisms have provided many inspirations, and bionics has helped many scholars to recognize the amazing properties of drag reduction on the surface of organisms, the most famous of which is shark skin drag reduction. Oeffner and Lauder (2012) showed that the tiny groove-like structures on the shark skin surface could enhance the adsorption of the leading edge of the blunt body structure to make the shark swim faster. A closer look at the shark skin surface structure revealed that these small groove-like structures are not of a single scale and that such structures can effectively increase thrust and reduce drag. It is applied to the cylindrical surface in this study to investigate its wake structure. The construction of single-v-grooved structures has been

the topic of earlier research; this study creates a novel type of grooved cylinder that includes a second groove in addition to the first. In this paper, the differences in their wake characteristics are studied and compared with secondary grooved cylinders of different depths. This research is beneficial to improve the safety and stability of marine structures and provide theoretical support and a practical basis for the application of marine structures. Therefore, secondary trench cylinders of different depths are of high research value as the target of this study.

The objective of this study is to measure the flow field velocities and wake characteristics in the flow plane and spanwise plane for smooth cylinder and secondary grooved cylinders with different depths by the particle image velocimetry (PIV) technique. The fluctuation of the wake structure of secondary grooved cylinders with different depths is the main topic of this work, including time-averaged streamlines, time-averaged velocity, RMS velocity, Reynolds stress, turbulent kinetic energy, instantaneous flow structures and spectral characters.

2. EXPERIMENTAL APPARATUS

The experiments were performed in a recirculating water tank in the PIV particle lab, which used to display the cylindrical wake using PIV technology, the field schematic is shown in Fig. 1. The experimental part has a rectangular cross-section that is 0.3 meters wide by 0.4 meters high, so the cross-sectional area S of the experimental section of the tank is 0.12m^2 . The console controls the quantity of flow, thus controlling the flow velocity. The experiments were carried out at a flow rate of $165\text{ m}^3/\text{h}$, corresponding to a flow rate of 0.382 m/s according to the experimental model, and its corresponding Reynolds number is $Re=7640$.

The material of the cylinder in the experiment is PVC, and its length (L) is 300mm , and diameter (D) is 20mm . In other words, the cylinder's length to diameter ratio is $15:1$. This ratio is big enough to guarantee the two-dimensional flow is visible in the cylinder's near-tailing region. The blockage ratio is less than 5%. The cross-sectional schematic of the cylinder is shown in Fig. 2. Case 1 shows a smooth cylinder, and Case 2 shows 16 original grooves

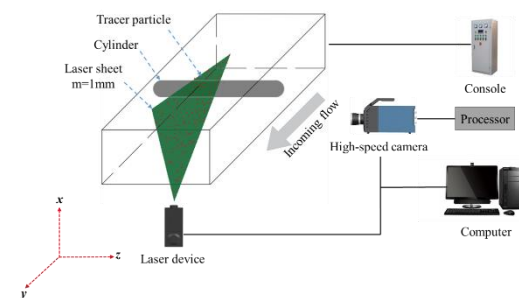


Fig. 1. PIV particle circulation water tank experiment.

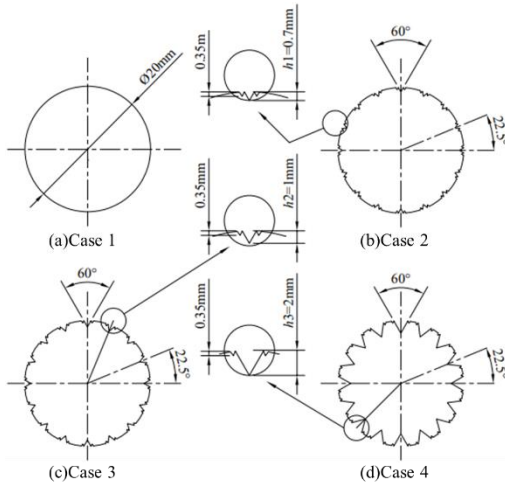


Fig. 2. Schematic diagram of the cylinder cross-section. (a) Case1: smooth cylinder, (b) Case2: secondary grooved cylinder with $h/D=0.035$, (c) Case3: secondary grooved cylinder with $h/D=0.05$, (d) Case4: secondary grooved cylinder with $h/D=0.1$.

evenly distributed on the surface of the cylinder, each groove angle is 60° , and the original groove depth (h) is 0.7mm, based on which one secondary groove of 0.35mm depth is arranged on both sides of each original groove. The only difference between Case 2, Case 3, and Case 4 is the depth of the original groove; all other dimensions are left unaltered. The original groove depth in Case3 is 1 mm and in Case4 is 2 mm. Case2, Case3, and Case4 are designed to simulate the shark epidermal structure (Oeffner and Lauder 2012). Takayama and Aoki (2005) studied grooved cylinders with $h/D = 0.0175$ (h/D is the surface roughness coefficient, where D is the diameter of the cylinder and h is the roughness height) and improved the drag reduction impact. Talley and Mungal (2002) studied grooved cylinders with $h/D=0.035$, Zhou *et al.* (2015c) studied grooved cylinders with $h/D=0.05$, and Afroz and Sharif (2022) studied grooved cylinders with $h/D=0.1$, which also achieved good resistance reduction. In this paper, combining these four conditions, the groove depths of the original grooves were 0.7 mm ($h/D=0.035$), 1 mm ($h/D=0.05$), and 2 mm ($h/D=0.1$), and the groove depths of the small grooves were all 0.35 mm ($h/D=0.0175$). This groove structure is similar to the groove-like structures of different scales on the surface of sharks; the structure is the focus of this study.

A high-speed camera, tracer particles, a light source, and an image processing system are the main elements of the PIV system. The high-speed camera used in this experiment has a resolution of 1008×1008 pixels and records 4000 successive digital particle pictures at a time interval of 0.5ms, or 2000 frames per second (fps), with a $1.5\mu s$ exposure period for each frame. The experiment uses a high-speed camera to continuously capture 12000 digital particle images in 6s, which is used to analyze the flow characteristics of the flow field. The average particle diameter of the PIV tracer particles used in

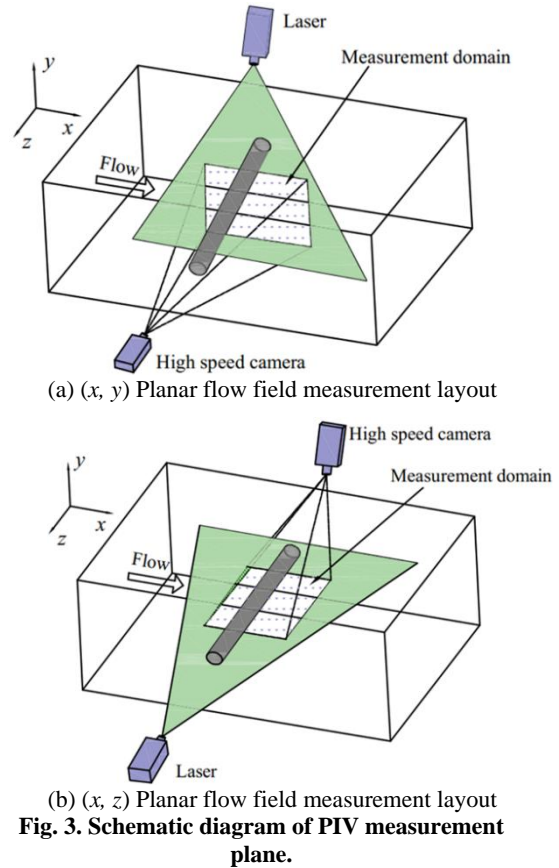


Fig. 3. Schematic diagram of PIV measurement plane.

this experiment is $10\mu m$, which can show the water flow characteristics very well.

Figure 3 shows a schematic diagram of the PIV measurement plane, using the PIV measurement technique to collect flow field data in the (x, y) plane and (x, z) plane of the cylindrical wake, respectively. The directions of the lateral and longitudinal directions, as well as the flow direction, are denoted by the coordinates x , y , and z . The data are measured in the spreading plane (x, z) and the flow direction plane (x, y) , as illustrated in Fig. 3(a) and (b), respectively. The experimental cylinder was installed in the sink of the experimental section, and the placement of the experimental cylinder was shown schematically in Fig. 4, the base of the cylinder, with the origin of the two-dimensional plane pointing in the direction of the water flow along the middle channel plane.

3. RESULTS AND DISCUSSION

3.1 Time-Averaged Streamlines and Velocity Field

Figure 5 presents a comparison of the time-averaged streamline and the time-averaged streamwise velocity \bar{u}/U contours in the (x, y) -plane of $z=0$ for a smooth cylinder and secondary grooved cylinders with different depths. In each case, a few symmetrical streamwise vortices were seen in the region of the cylinder's wake, encircled by shear layers from the cylinder's two sides (Sumner 2016).

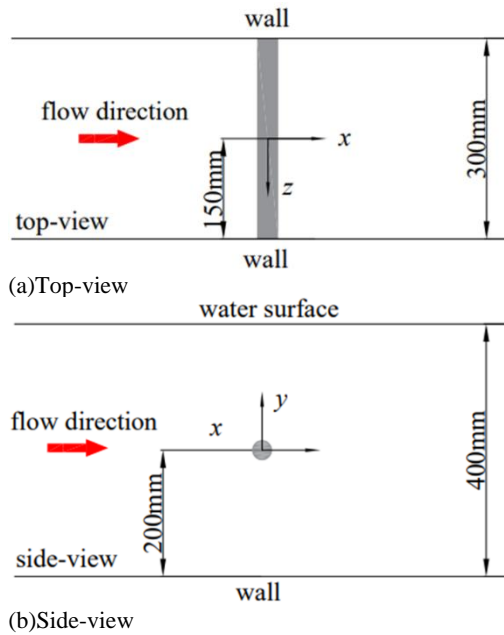


Fig. 4. Schematic diagram of the placement of the experimental cylinder.

Figure 5(a) shows a smooth cylinder with a recirculation zone of $1.906D$. Figures 5(b), (c) and (d) show secondary grooved cylinders with different depths with recirculation zones of $1.572D$, $1.433D$ and $1.614D$, respectively, which indicates that the length of the recirculation zone is reduced by 17.5%, 24.8% and 15.3%, respectively (Zhou *et al.* 2015a). This shows a larger recirculation zone for the smooth cylinder, and the length and width are larger than those of the secondary grooved cylinders with different depths. The reason for this may be that the original groove structure and the secondary groove structure change the position of the boundary layer separation point, which makes the boundary layer separation point position move backward, resulting in the reduction of the recirculation zone. Another factor is the formation of a huge number of small vortices inside the secondary groove structure, and the presence of small vortices interferes with the development of large vortices and destabilizes the wake region (Zhu 2017). In addition, the presence of a tip structure (top corner of the groove) between the large and small grooves in the secondary groove cylinder causes the large vortices to be broken into small vortices, which means that the secondary groove structure on the surface of the cylinder can reduce the scale of the large vortices and affect the size of the recirculation region (Fujisawa *et al.* 2020). In comparison to secondary grooved cylinders with different depths, the secondary grooved cylinder with $h/D=0.05$ has the least length and breadth of the recirculation area, which is due to the stronger interference of small-scale vortices in the secondary groove at that depth to the large-scale vortices in the original groove. The large-scale vortices are broken into more small-scale vortices.

The above results (Fig. 5) show that the formation of vortices is suppressed by the secondary groove

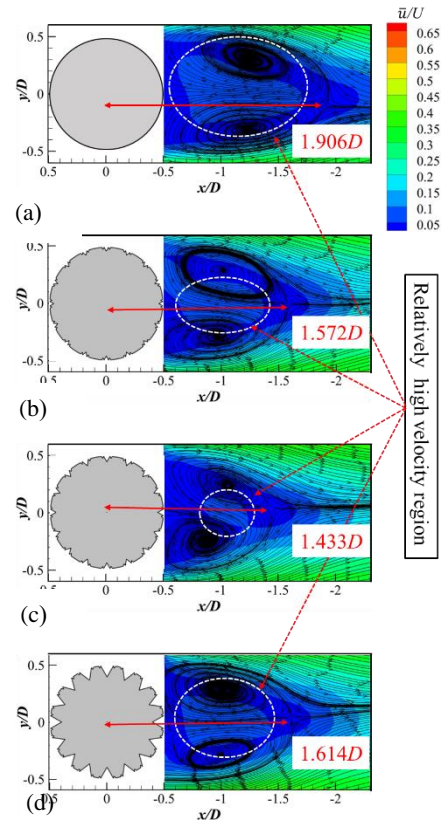


Fig. 5. The time-averaged streamlines and the streamwise velocity contours in the (x, y) -plane. (a) smooth cylinder, (b) secondary grooved cylinder with $h/D=0.035$, (c) secondary grooved cylinder with $h/D=0.05$, (d) secondary grooved cylinder with $h/D=0.1$.

structure, causing a substantial decrease in the recirculation zone, which may be related to the reduction in the drag force applied to the cylinder (Rinoshika and Rinoshika 2018).

A schematic diagram of the velocity extraction locations in the wake region is shown in Fig. 6. The flow velocities at six positions close to the cylinder in the wake zone were retrieved and compared in order to evaluate the velocity fluctuation in the cylinder's wake in the experiment. The six places are $x/D=0.8$ in position A, $x/D=1.1$ in position B, $x/D=1.6$ in position C, $x/D=2.6$ in position D, $x/D=3.6$ in position E, and $x/D=4.6$ in position F.

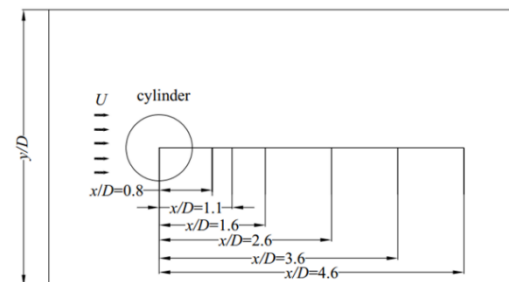


Fig. 6. Schematic diagram of wake velocity extraction location.

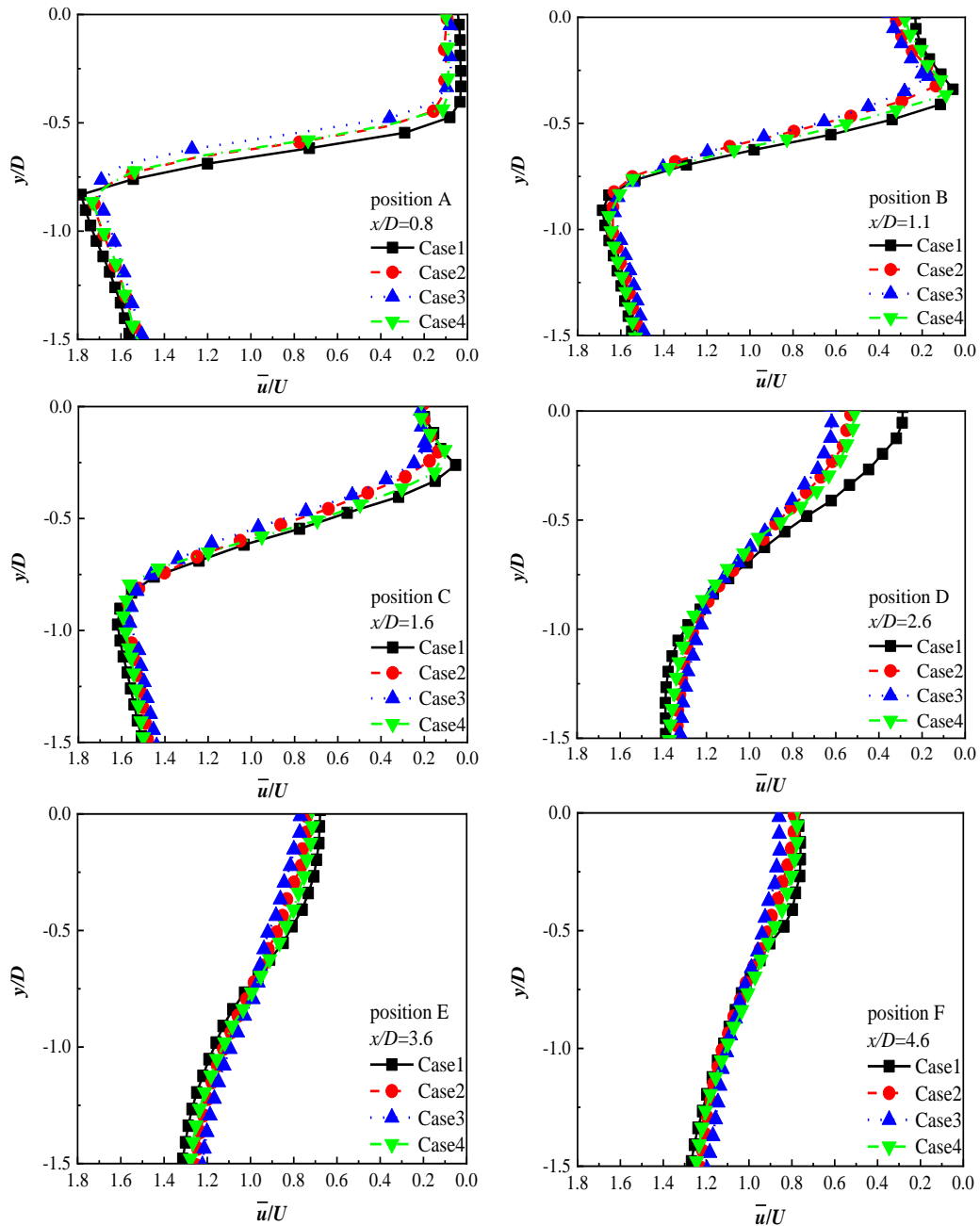


Fig. 7. The profiles of time-averaged streamwise velocity in the (x, y) -plane.

These velocity profiles were used for stability analysis, provided flow velocity does not vary significantly along the flow direction (Baek and Karniadakis 2009). Figure 7 plots the time-averaged velocity profiles of the wake at different positions in the (x, y) plane for a smooth cylinder and secondary grooved cylinders with different depths. Since the time-averaged velocities are symmetrically distributed around the centerline of $y/D = 0$, only half of the time-averaged velocities are plotted here, as shown in Fig.7.

At position A, the wake velocity of the smooth cylinder is larger compared to the secondary grooved cylinder with different depths in the range of $-1.5 < y/D < -0.8$ because the adsorption of vortices by the secondary groove structure slows down the velocity

of the fluid outside the shear layer. The secondary grooved cylinders with different depths and the smooth cylinder experience a rapid decrease in velocity in the wake zone for $-0.8 < y/D < -0.5$, which is a result of the inherent characteristics of cylindrical bypass wake. The fluid velocity remains relatively stable for $-0.5 < y/D < 0$ because the low-velocity wake region has a certain width. Additionally, it is discovered that the wake velocity of the smooth cylinder is lower than that of the secondary grooved cylinders with different depths at $-0.8 < y/D < 0$, indicating that the secondary groove structure changes the velocity distribution in the wake basin and reduces the velocity gradient, especially the secondary grooved cylinder with $h/D=0.05$ has a more obvious effect on velocity control. The wake

zone width of the secondary grooved cylinder with $h/D=0.05$ was the smallest, and it was also discovered that the wake zone widths of the secondary grooved cylinders with different depths were less than those of the smooth cylinder. This is because the secondary groove structure at this depth has a stronger adsorption effect on the vortex, which makes the vortex shedding delayed and the shedding location more concentrated at the trailing edge of the cylinder.

Position B causes a change in the velocity profile's shape for secondary grooved cylinders with different depths and the smooth cylinder, and the variation of fluid velocity in the range $-1.5 < y/D < -0.5$ is consistent with the velocity trend at position A. For $-0.5 < y/D < 0$, the width of the time-averaged velocity distribution at position B for the smooth cylinder and secondary grooved cylinders with different depths tends to decrease compared to that at position A. This is because as the monitoring distance moves away from the center of the cylinder, the vortex after shedding develops along the downstream direction, and the effect on the longitudinal direction gradually decreases, comparing position C and position D, this phenomenon is more obvious, which is related to the reduction of recirculation zone. It is also found that the fluid velocity of both the smooth cylinder and the wake of the secondary grooved cylinders with different depths in the low-velocity wake region is significantly higher at position B compared to position A. This means that a part of the additional high-velocity zone is formed in the middle of the low-velocity zone, as shown in Fig. 5, the smooth cylinder's high-velocity zone is bigger than the high-velocity zones of secondary grooved cylinders with different depths, especially the size of the high-velocity zone of the secondary grooved cylinder with $h/D=0.05$ is the smallest. This indicates that the secondary groove structure at that depth compresses the larger size of the high flow velocity zone, which is related to the reduced area of the recirculation zone.

At position C, the wake velocity of the smooth cylinder reaches a minimum in the range $-0.3 < y/D < 0$ and then starts to rise, because the extracted velocity profile line passes through a relatively high-velocity region. In contrast, the width of the low-velocity region narrows for the smooth cylinder and secondary grooved cylinders with different depths, which is associated with the reduced width of the recirculation region.

It is evident at position D that the secondary grooved cylinders' velocity gradients are less than those of the smooth cylinder, which may be attributed to the attachment of the fluid in the secondary grooves, slowing down the reduction of the wake velocity, especially the secondary grooved cylinder with $h/D=0.05$ has the greatest effect on the velocity.

The velocity gradient of the flow decreases from position E to position F. This is because the extracted velocity profile line is far from the cylindrical wall surface, and the wake is less affected. However, it can still be seen that the secondary groove structure

affects the wake velocity, with the secondary grooved cylinder with $h/D=0.05$ having the greatest effect. It was also found that at position F, the difference in wake velocity between a smooth cylinder and secondary grooved cylinders with different depths was not significant, indicating that the distribution of wake velocity at this position was no longer affected by the depth of the secondary groove, which mainly affected the velocity distribution in the range of $x/D = 0$ to 4.6.

As shown in Fig. 7, the effect of the cylinder on the wake velocity gradually decreases in the wake region from position A to position F (Aguedal *et al.* 2018). The velocity gradients of the secondary grooved cylinders with different depths are also at all positions smaller compared to the smooth cylinder. This phenomenon is more obvious in the secondary grooved cylinder with $h/D=0.05$, which is due to the stronger interference of the small-scale vortices in the secondary groove with the large-scale vortices in the original groove at this depth, and the secondary groove structure at this depth can better reduce the scale of the large vortices, which are broken into more small-scale vortices, resulting in a significantly smaller recirculation zone at this depth.

To further understand the flow field, a PIV visualization of the flow field of the cylindrical spreading (Law and Jaiman 2018) structure was performed in this study. Figure 8 compares the time-averaged streamlines and time-averaged velocities for a smooth cylinder at $y/D = 0$ in the (x, z) plane and secondary grooved cylinders with different depths. Figure 8(a) shows the time-averaged flow line diagram and the time-averaged velocity profile for the smooth cylinder, a reversed flow region approximately parallel to the cylindrical wall, characterized by a negative flow direction of the internal velocity (Zheng and Rinoshik 2020) and no vortex formation in the reversed velocity flow line, which is different from the vortex flow line structure in the (x, y) plane. At the position of $x/D = 1.624$, the flow velocity at the tail of the smooth cylinder is approximately zero, and the distance from the cylinder surface to $1.624D$ is referred to as the formation length of the reflux zone. And downstream of $x/D = 1.624$, the flow velocity gradually returns to the fluid velocity outside the wake region. The locations of the backflow zone dividers in Fig. 8(b), (c) and (d) are approximately $x/D = 1.31, 1.205$ and 1.488 , respectively. In contrast to the smooth cylinder, the formation length of the return zone is reduced for the secondary grooved cylinders with different depths, which also means that the negative flow velocity region is compressed. The wavy recirculation zone can be found in secondary grooved cylinders with different depths. This may be due to the re-broken connection of vortex division, i.e. wave shedding (Cao and Tamur 2015). The above phenomenon indicates that the introduction of the secondary groove structure significantly changes the structure of the near wake region, leading to a reduction in the formation length of the vortex, especially for the secondary grooved cylinder with $h/D=0.05$.

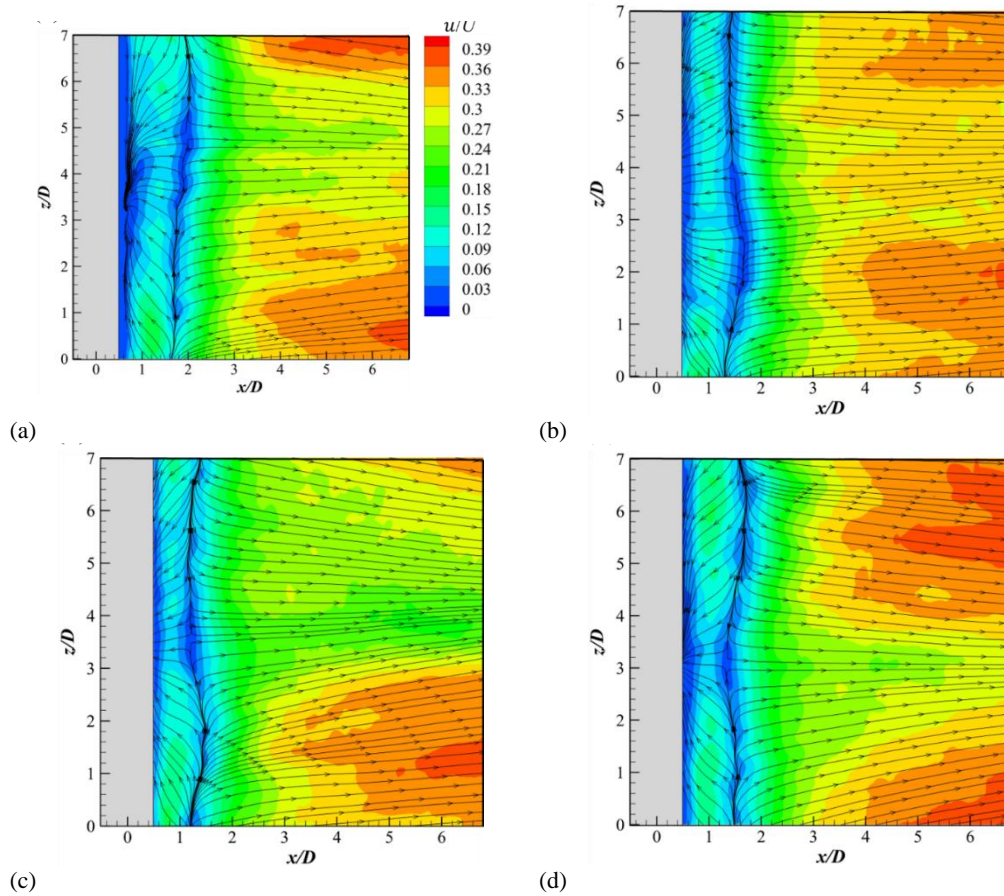


Fig. 8. Time-averaged velocity streamlines in the (x, z) -plane. (a) smooth cylinder, (b) secondary grooved cylinder with $h/D=0.035$, (c) secondary grooved cylinder with $h/D=0.05$, (d) secondary grooved cylinder with $h/D=0.1$.

Figure 9 plots the time-averaged spreading velocity distributions at six positions $y = 0$ for $x/D = 0.8$ (position A), 1.1 (position B), 1.6 (position C), 2.6 (position D), 3.6 (position E) and 4.6 (position F), respectively. Two flow lines with velocities close to zero are observed in Fig. 8, namely the cylindrical wall and the return boundary line.

At position A, the time-averaged velocity of the smooth cylinder is lower than the time-averaged velocity of the secondary grooved cylinders with three different depths due to the expansion of the streamline region where the velocity tends to zero, which reduces the velocity in the region near the smooth cylinder.

At position A and position B, the flow velocity is relatively low. Still, its fluctuation is large, as shown in Fig. 9, which is because both positions are in the reflux zone, and the fluid velocity is unstable. The velocity on both sides is significantly greater than the velocity in the middle position, which is consistent with the velocity field phenomenon in the reflux zone shown in Fig. 8. This may be influenced by the length of the cylindrical spreading. There is a certain error in the measurement calculation, which makes the final velocity results more variable.

From position A to position B, the smooth cylinder's time-averaged velocity value grows, but the value of the time-averaged velocity of the secondary grooved

cylinders with different depths decreases because, at position A, the smooth cylinder is closer to the cylindrical wall with velocity 0, while the secondary grooved cylinders with different depths are farther from the flow line with velocity 0 on both sides. In position B, the opposite is true, as the smooth cylinder is farther from the flow line with velocity 0 on both sides. In contrast the secondary groove cylinders with different depths are closer to the return flow boundary line with velocity 0.

At position C, the profile line of the smooth cylinder is close to the return boundary line, while the secondary grooved cylinders with different depths are farther away from the flow line with velocity 0 on both sides; therefore, the time-averaged flow velocity of the smooth cylinder is lower than that of the secondary grooved cylinders with different depths.

At position D, the velocity of the smooth cylinder is significantly lower than that of the secondary grooved cylinders with different depths, which means that the smooth cylinder is closer to the return boundary line. The results show that the secondary groove structure affects the length of the reflux zone, which in turn affects the flow velocity distribution. At position E, the time-averaged velocity is less influenced by the surface of the cylinder, and the velocity fluctuates around 0.8. At position F, the

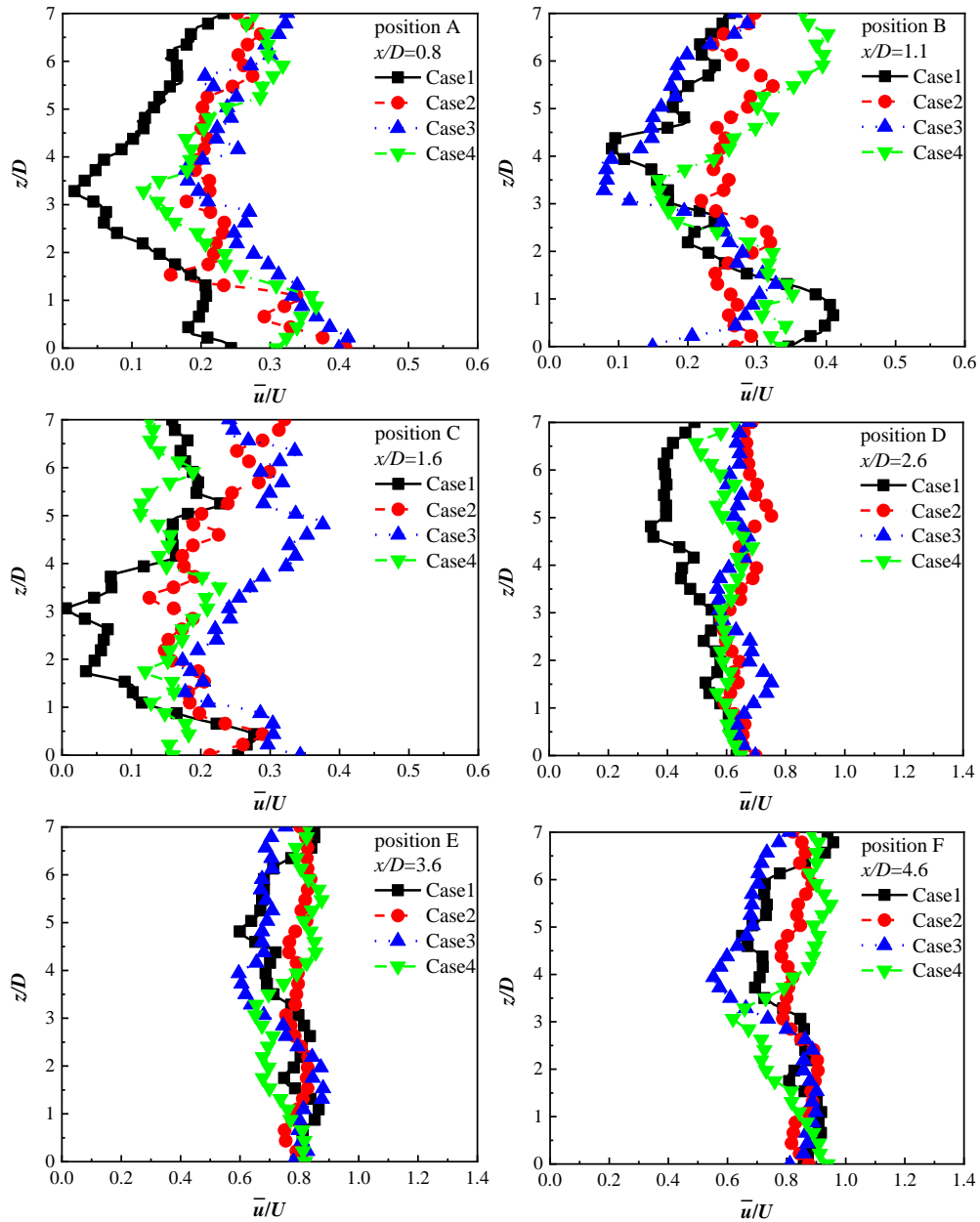


Fig. 9. The profiles of time-averaged streamwise velocity in the (x, z) -plane.

time-averaged velocity gradually returns to the incoming velocity, and the normalized velocity is stabilized between 0.6 ~ and 1. This also implies a reduction in the wake's impact on the smooth cylinder and secondary grooved cylinders with different depths.

On the other hand, comparing the time-averaged velocities at the six positions, it can be found that the time-averaged velocity of the smooth cylinder increases slightly from position A to position B. From position C to position F, the time-averaged velocities of the smooth cylinder and secondary grooved cylinders with different depths increase significantly, and this phenomenon is more obvious at position F, indicating that the cylindrical model little influences the wake velocity at this position. And for the comparison of secondary grooved

cylinders with different depths, no significant difference was found.

3.2 Root Mean Square (Rms) Velocity

A detailed qualitative analysis of the time-averaged velocities has been presented above, showing that the secondary groove structure affects the wake velocity. However, the root-mean-square treatment of the velocities allows a numerical quantitative analysis to make the results more straightforward.

Contour plots of the flow direction and lateral root mean square (RMS) velocity fluctuation intensity in the (x, y) plane for a smooth cylinder and secondary grooved cylinders with different depths are shown in Fig. 10 and Fig. 11, respectively. The velocity pulsation components u' and v' are rms-processed to

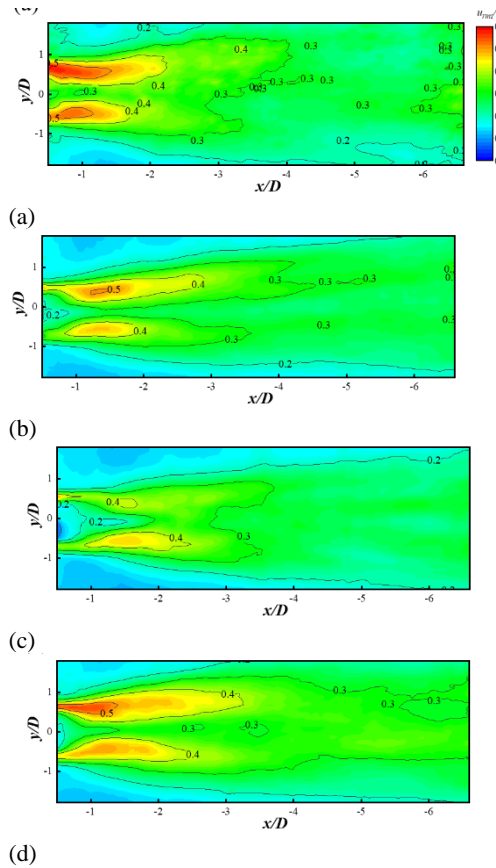


Fig. 10. RMS streamwise velocity distribution in the (x, y) -plane. (a) smooth cylinder, (b) secondary grooved cylinder with $h/D=0.035$, (c) secondary grooved cylinder with $h/D=0.05$, (d) secondary grooved cylinder with $h/D=0.1$.

obtain the velocity pulsation intensity, with u' and v' denoting the flow along the flow direction and transverse direction, respectively. As shown in Fig. 10(a), along the time-averaged separation line, the peak of the directional flow root mean square (RMS) velocity fluctuation intensity of the smooth cylinder in the near wake region reaches $u_{rms}/U = 0.591$. The peak root mean square (RMS) velocity fluctuation intensities in Fig. 10(b), (c) and (d) are 0.509, 0.467 and 0.563, respectively. In contrast to the smooth cylinder, the peak velocity fluctuation intensity of flow direction is reduced for secondary grooved cylinders with different depths, especially for the secondary grooved cylinder with $h/D=0.05$. This is due to the geometry of the secondary grooves on the cylindrical surface.

It is noteworthy that the location of the appearance of the peak intensity of the flow velocity fluctuations is delayed in the flow direction for secondary grooved cylinders with different depths compared to the smooth cylinder, especially for the secondary grooved cylinder with $h/D=0.05$ by $1D$. This may be due to the slower growth of vortices within the shear layer of secondary grooved cylinders and the suppression of the vortex-shedding process in the near-wake flow (Liu *et al.* 2011).

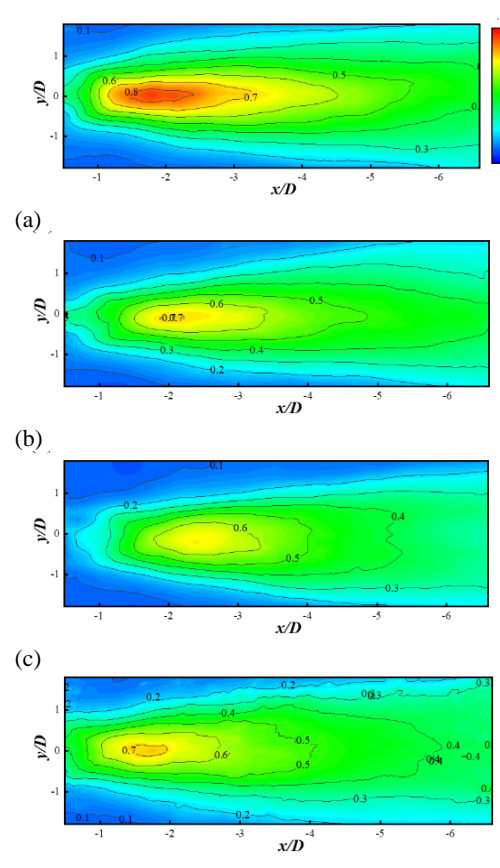


Fig. 11. Transverse root mean square (RMS) velocity distribution in the (x, y) -plane. (a) smooth cylinder, (b) secondary grooved cylinder with $h/D=0.035$, (c) secondary grooved cylinder with $h/D=0.05$, (d) secondary grooved cylinder with $h/D=0.1$.

The distribution of the transverse velocity fluctuation intensity also has a similar trend. As shown in Fig. 11(a), the smooth cylinder's peak transverse velocity fluctuation intensity is $v_{rms}/U = 0.84$. While the peak values of transverse velocity fluctuation intensity for secondary grooved cylinders with different depths are 0.705, 0.686, and 0.72, respectively, as shown in Fig. 11(b), (c), and (d). In addition, the locations of the peak transverse velocity fluctuation intensities of the secondary grooved cylinders with different depths are delayed in the flow direction compared to the smooth cylinders, especially the secondary grooved cylinder with $h/D=0.05$ delayed by $0.6D$.

Significant differences in the magnitude and location of the peaks in the intensity of flow velocity fluctuations and lateral velocity fluctuations indicate that the development of the vortex downstream in the cylindrical near-tail flow region is suppressed, which favors the reduction of the lateral drag of the cylinder. Thus, the presence of the secondary groove structure on the cylindrical surface weakens the growth rate of the vortex in the shear layer and delays the formation of the Carmen vortex street (Liu *et al.* 2011), hence shortening the recirculation zone, as shown in Fig. 5.

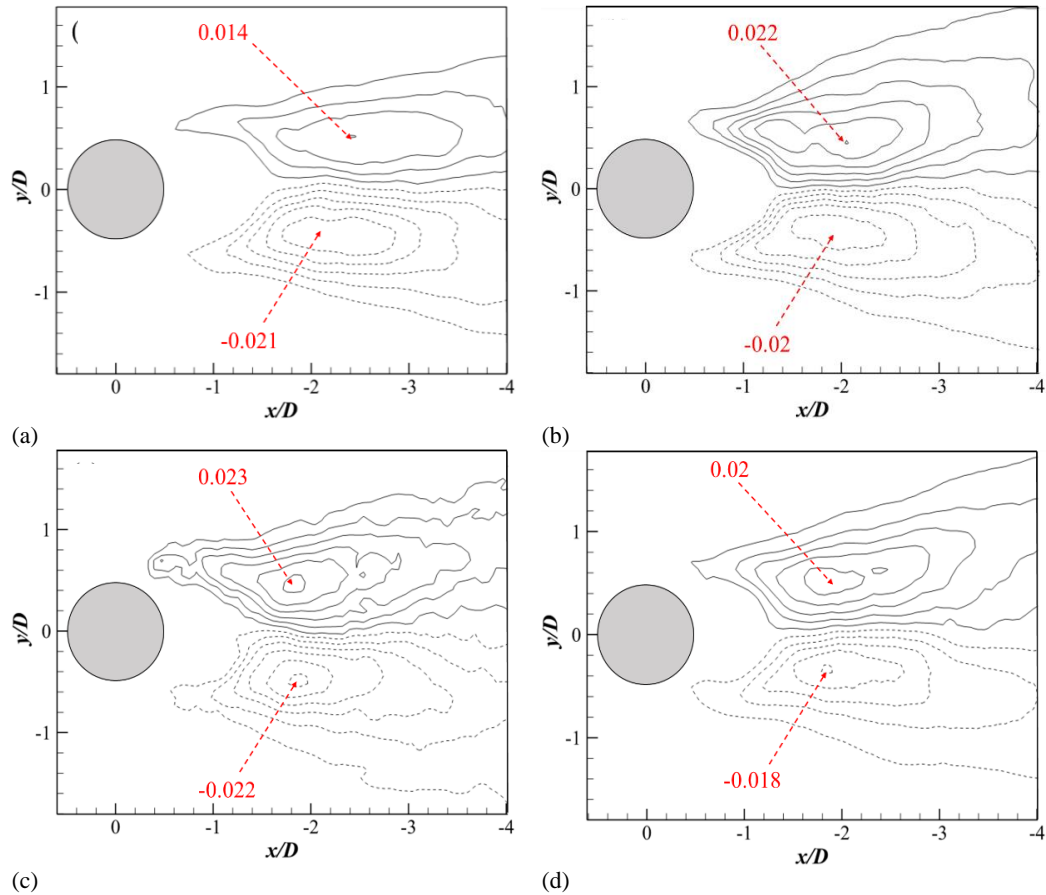


Fig. 12. Contours of the normalized Reynolds stress $\overline{u'v'}/U^2$ in the (x, y) -plane at $z/D=0$. (a) smooth cylinder, (b) secondary grooved cylinder with $h/D=0.035$, (c) secondary grooved cylinder with $h/D=0.05$, (d) secondary grooved cylinder with $h/D=0.1$.

3.3 Reynolds Stress

Reynolds stress and turbulent kinetic energy (TKE) are important parameters reflecting the variation of the flow field. Therefore, in this section, Reynolds stress and turbulent kinetic energy (TKE) contour maps are plotted to study the flow field characteristics of smooth cylindrical and three secondary grooved cylindrical surfaces with different depths.

The Reynolds stress results from adding the mean value against time and the pulse value of all physical parameters in turbulent flow. Understanding the stress distribution connected to the flow field is made easier by analyzing the Reynolds stress. Fig. 12 shows the normalized Reynolds stress distribution in the (x, y) plane for a smooth cylinder and secondary grooved cylinders with different depths. It can be seen from the figure that the Reynolds stresses in all cases are symmetrically distributed near the centerline of the cylindrical wake, as shown in Fig. 12(a). Two Reynolds stress regions with opposite positive and negative values are observed in the wake region of the smooth cylinder, with the largest positive value of 0.014 and the largest negative value of -0.021. The positive and negative values represent the direction only. As shown in Fig. 12(b), (c), and (d), the maximum Reynolds stress values for the secondary grooved cylinders with different depths

are about 0.022, 0.023, and 0.02, respectively, which indicate that the maximum Reynolds stress values are increased by 57.1%, 64.3% and 42.9%, respectively, and their minimum Reynolds stress values are about -0.02, -0.022 and -0.018, respectively. In contrast to the smooth cylinder, the maximum Reynolds stress values are increased for secondary grooved cylinders with different depths. This is due to the secondary groove structure's impact on the change of the flow structure in the cylinder's wake region, where the tip structure also plays an important role in increasing the turbulent fluctuations within the boundary layer (Rinoshika and Rinoshika 2019). And the maximum Reynolds stress value increases the most for the secondary grooved cylinder with $h/D=0.05$, indicating that the original groove's depth also has a significant effect. So that the Reynolds stress and recirculation zone of the secondary grooved cylinders with different depths were controlled, as shown in Fig. 5 and Fig. 8.

Figure 13 shows the Reynolds stress distribution in the (x, z) plane for a smooth cylinder and secondary grooved cylinders with different depths. As shown in Fig. 13(a), it is observed that the positive and negative Reynolds stress regions appear at the wake of the smooth cylinder with a maximum positive value of 0.003 and a maximum negative value of -0.005.

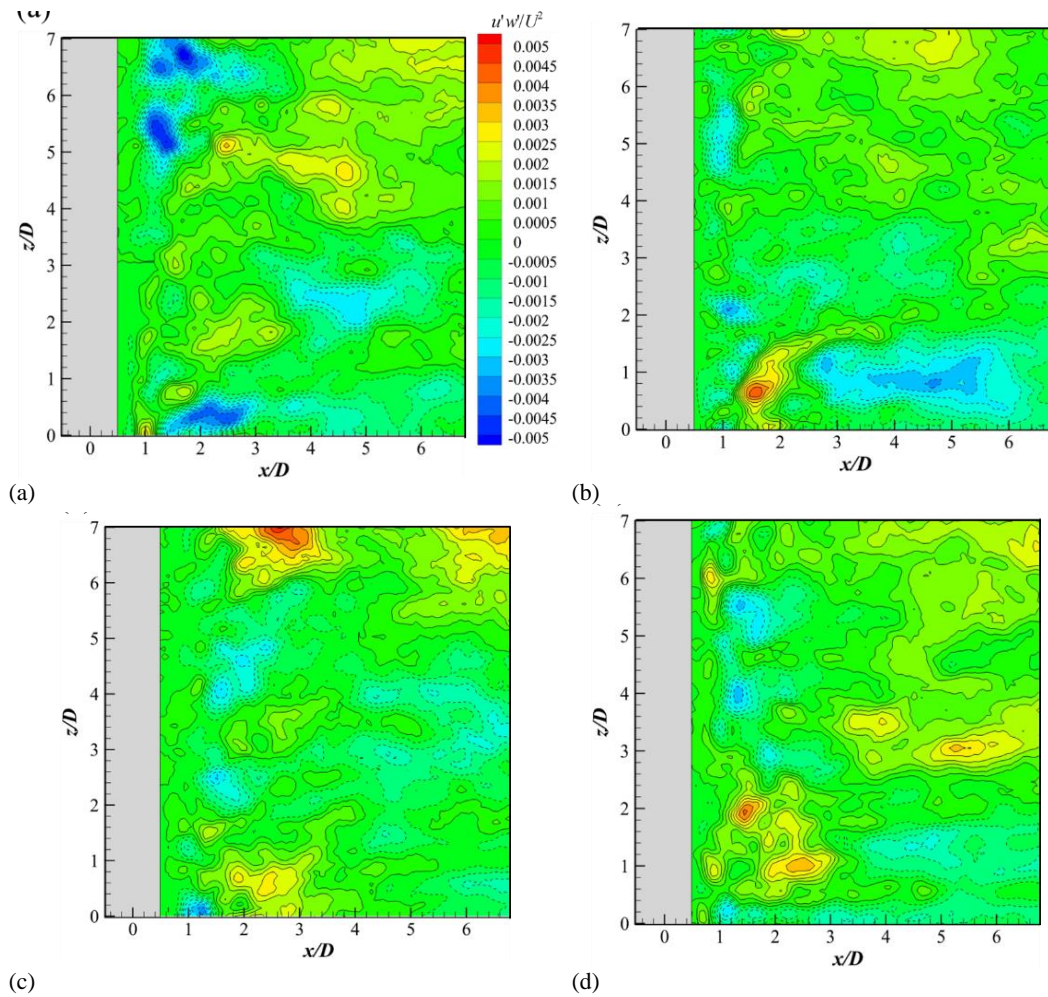


Fig. 13. Contours of the Reynolds stress $\overline{u'w'}/U^2$ in the (x, z) -plane at $y/D=0$. (a) smooth cylinder, (b) secondary grooved cylinder with $h/D=0.035$, (c) secondary grooved cylinder with $h/D=0.05$, (d) secondary grooved cylinder with $h/D=0.1$.

As shown in Fig. 13(a), there are three negative Reynolds stress regions in the smooth cylinder's wake region with a maximum negative value of -0.005. It can be seen in Fig. 13(c) and (d) that the Reynolds stress gradually increases, and an obvious high-stress zone appears during the downstream movement of the tail flow for the secondary groove cylinder with $h/D=0.05$ and the secondary groove cylinder with $h/D=0.1$. The positive maximum Reynolds stress values for the secondary grooved cylinders with different depths were 0.004, 0.005, and 0.004, respectively, as shown in Fig. 13(b), (c), and (d). In contrast to the smooth cylinder, the Reynolds stress maximum values after secondary grooved cylinders with different depths are slightly increased, especially for the secondary grooved cylinder with $h/D=0.05$. This could be connected to how the secondary groove structure affects the flow characteristics.

3.4 Turbulent Kinetic Energy

On the other hand, turbulence intensity is measured using turbulent kinetic energy (TKE), which is directly connected to the momentum and energy flow

inside the boundary layer. Figure 14 shows the normalized TKE distribution in the (x, y) plane for a smooth cylinder and secondary grooved cylinders with different depths. As shown in Fig. 14(a), the smooth cylinder's maximum turbulent kinetic energy value is 0.084. As shown in Fig. 14(b), (c), and (d), the maximum values of turbulent kinetic energy are 0.094, 0.114, and 0.085 for the secondary grooved cylinders with different depths, which indicate that the maximum values of turbulent kinetic energy are reduced by 11.9%, 35.7%, and 1.2%, respectively. In contrast to the smooth cylinder, the TKE maxima after the secondary groove cylinders with different depths were increased. This could be because the secondary grooved cylinder prevents vortex formation in the wake zone, allowing for a rise in turbulent kinetic energy. The spiking effect of the secondary grooved cylinder causes the highest peak of TKE produced by fluid flow in the wake zone to rise, which causes the already formed large vortices to be broken into smaller ones (Zheng and Rinoshik 2020). The increase in TKE weakens the drag force acting on the cylinder (Lim and Lee 2003). In addition, the secondary grooved cylinder with $h/D=0.05$ has the

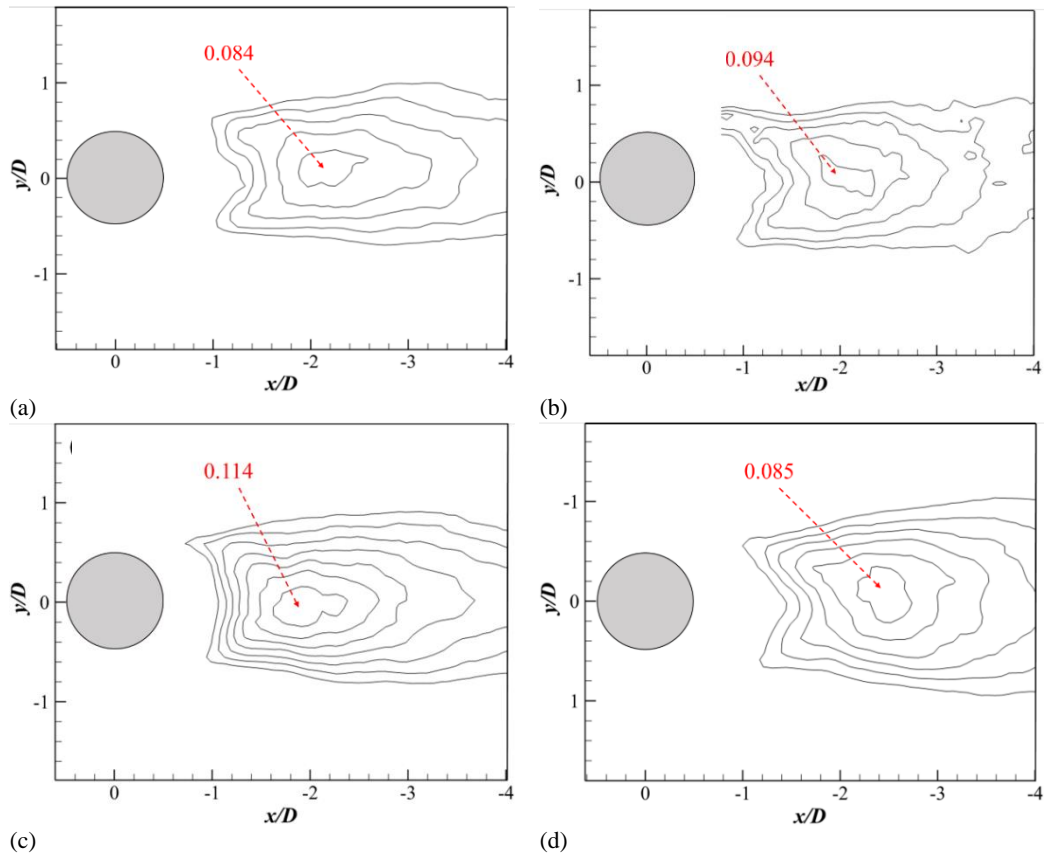


Fig. 14. Contours of the normalized turbulent kinetic energy in the (x, y) -plane at $z/D=0$. (a) smooth cylinder, (b) secondary grooved cylinder with $h/D=0.035$, (c) secondary grooved cylinder with $h/D=0.05$, (d) secondary grooved cylinder with $h/D=0.1$.

highest TKE maximum due to the stronger interference of small-scale vortices in the secondary groove at that depth to the large-scale vortices in the original groove, where the large-scale vortices are broken into more small-scale vortices.

Figure 15 shows the normalized TKE distribution in the spreading direction for a smooth cylinder and secondary grooved cylinders with different depths. As shown in Fig. 15(a), for the smooth cylinder, the high turbulence intensity region exists only on the lower side with a TKE maximum of 0.034. Fig. 15(b), (c), and (d) show that for the secondary grooved cylinders with different depths, the high turbulent kinetic energy region is concentrated on the upper or lower side with TKE maxima of 0.042, 0.052, and 0.035, respectively. Compared with the smooth cylinder, the TKE maxima after secondary grooved cylinders with different depths are slightly increased, especially for the secondary grooved cylinder with $h/D=0.05$. This may imply that the geometry of the secondary grooves increases the turbulence fluctuations and thus increases the turbulence intensity. The TKE results in Fig. 14 are qualitatively congruent with this. A phenomenon was also observed where the high turbulence intensity zone of the secondary grooved cylinder with $h/D=0.05$ extends downstream and has the largest extension area. This may be caused by the entrainment effect between the wake and the main flow, and the additional turbulent energy fluctuations caused by the secondary vortex structure.

Therefore, it can be said that the secondary groove structure's lowering of the recirculation zone is commensurate with a rise in Reynolds stress and turbulent kinetic energy, especially for the secondary grooved cylinder with $h/D=0.05$, as shown in Fig. 5.

3.5 Instantaneous Flow Structures

To compare the differences in flow structures in the wake flow between a smooth cylinder and secondary grooved cylinders with different depths, Fig. 16 shows typical instantaneous streamlines at $z/D = 0$ in the (x, y) plane. As shown in Fig. 16(a), two large vortices are observed at the wake flow of the smooth cylinder. As shown in Fig. 16 (b), (c), and (d), for secondary grooved cylinders with different depths, the scale of large vortices is affected by the backward shift of the boundary layer separation point. The cutting effect of the secondary groove structure leads to the partial splitting of large vortices into several small vortices in the wake region. However, the tip structure of the secondary groove causes the large vortices to continue to be split, so the small vortices in the wake region increase for the secondary grooved cylinders with different depths. This suggests that the development of small vortices is connected to the interior groove structure's effect on the wake flow. Comparing the secondary grooved cylinders with different depths, the secondary grooved cylinder with $h/D=0.05$ has the smallest vortices.

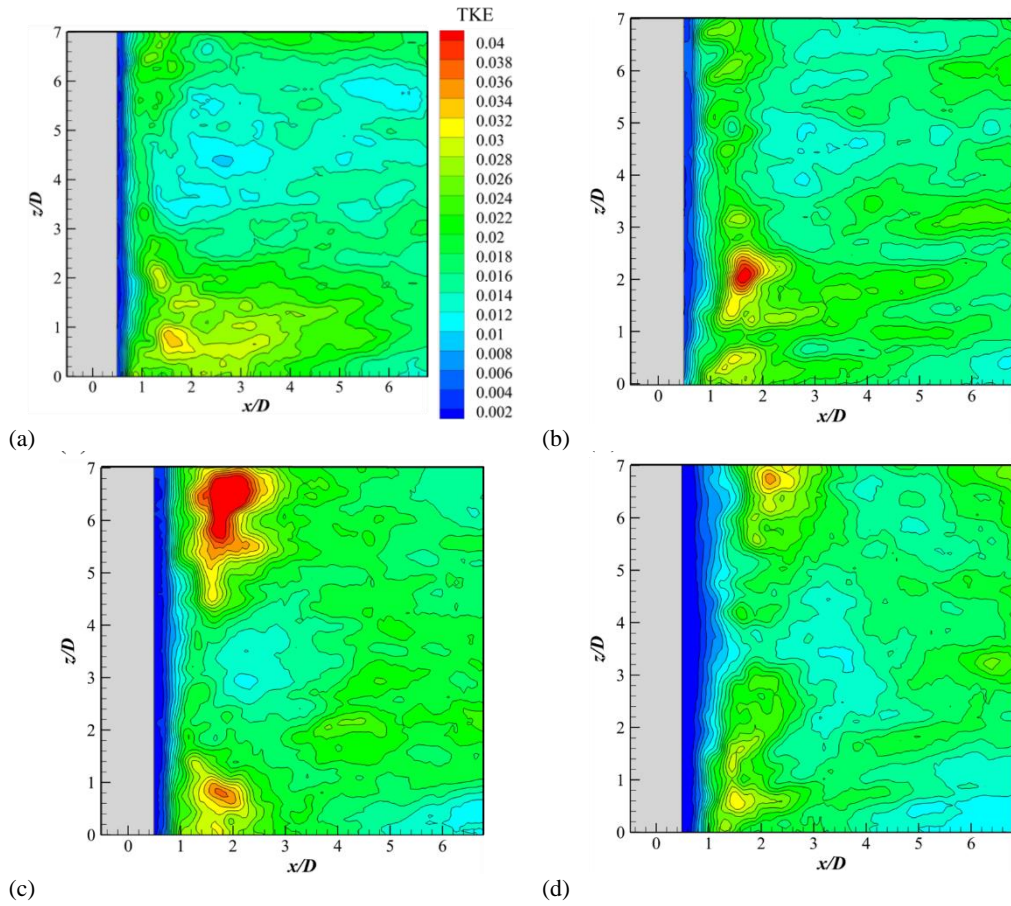


Fig. 15. Contours of the turbulent kinetic energy in the (x, z) -plane at $y/D=0$. (a) smooth cylinder, (b) secondary grooved cylinder with $h/D=0.035$, (c) secondary grooved cylinder with $h/D=0.05$, (d) secondary grooved cylinder with $h/D=0.1$.

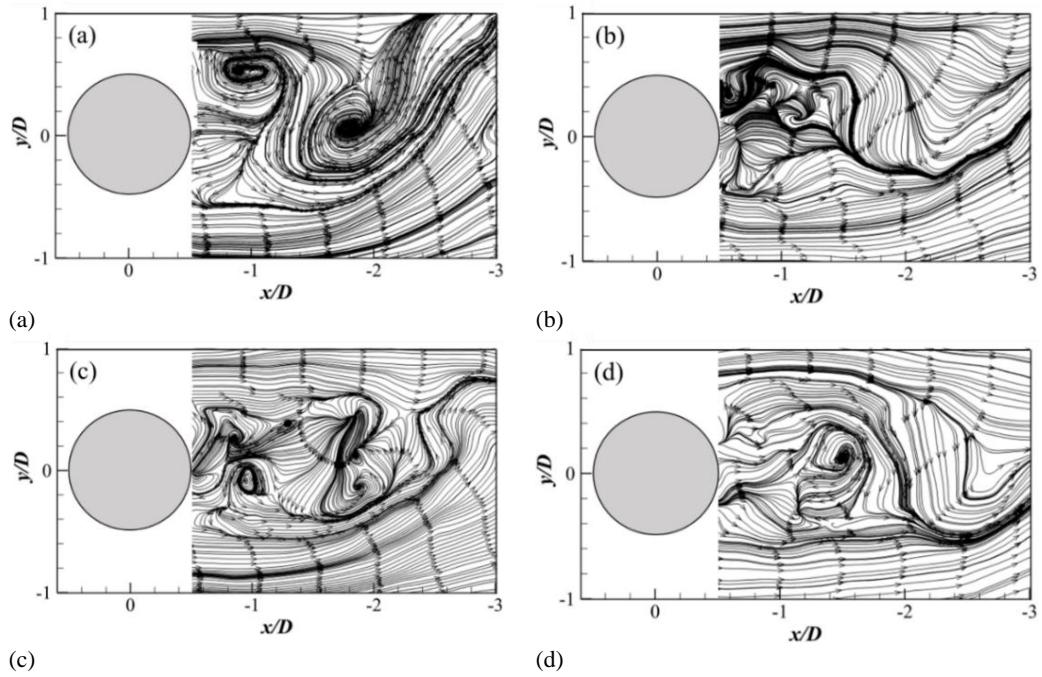


Fig. 16. Instantaneous streamlines in the (x, y) -plane at $z/D=0$. (a) smooth cylinder, (b) secondary grooved cylinder with $h/D=0.035$, (c) secondary grooved cylinder with $h/D=0.05$, (d) secondary grooved cylinder with $h/D=0.1$.

This is because the small-scale vortices in the secondary groove at this depth interfere more strongly with the large-scale vortices in the original groove, and the large-scale vortices are broken into more small-scale vortices.

Figure 17 plots typical instantaneous streamlines for smooth and secondary grooved cylinders with different depths at the (x, z) plane $y/D = 0$. As shown in Fig. 17 (a), a number of small vortices can be seen in the smooth cylinder's wake, which may be the result of the cylinder's spreading length's impact on the wake. Another reason could be the roll-sweep effect of the spreading shear layer in the near wake flow (Zhou *et al.* 2011). However, unlike the increase in vortices in the (x, y) plane wake region, the amount of small vortices in the spreading wake region decreases for secondary grooved cylinders with different depths, as shown in Fig. 17 (b), (c), and (d). This could be as a result of the small-scale vortices created by the secondary grooved cylinder and reattached to the inside of secondary groove structure during the return motion, resulting in a reduced amount of vortices. Comparing the secondary grooved cylinders with different depths,

the secondary grooved cylinder with $h/D=0.05$ has the least number of small vortices. This might be as a result of the small-scale vortices that are produced by the secondary grooved cylinder at this depth reattaching more to the interior of the secondary groove structure during reflux motion.

3.6 Spectral Characters

To further investigate the details of the flow structure, the spectra of 4000 pulsating velocity v points were calculated using PIV data. Fig. 18 depicts the spectrum S_V of the velocity component v in the wake of a smooth cylinder and secondary grooved cylinders with different depths at the location of $x/D = -1.2$ and $y/D = 0.3$. The measured positions are approximated to be located in the flow path to the vortex. Here, the relationship between the frequency f and the dimensionless Strouhal number St can be expressed as $St = fD/U$. As shown in Fig. 18(a), a large peak can be observed for the smooth cylinder, which corresponds to a frequency of $f = 4.007$ Hz. Therefore, $St = 0.21$ can be calculated from Eq.

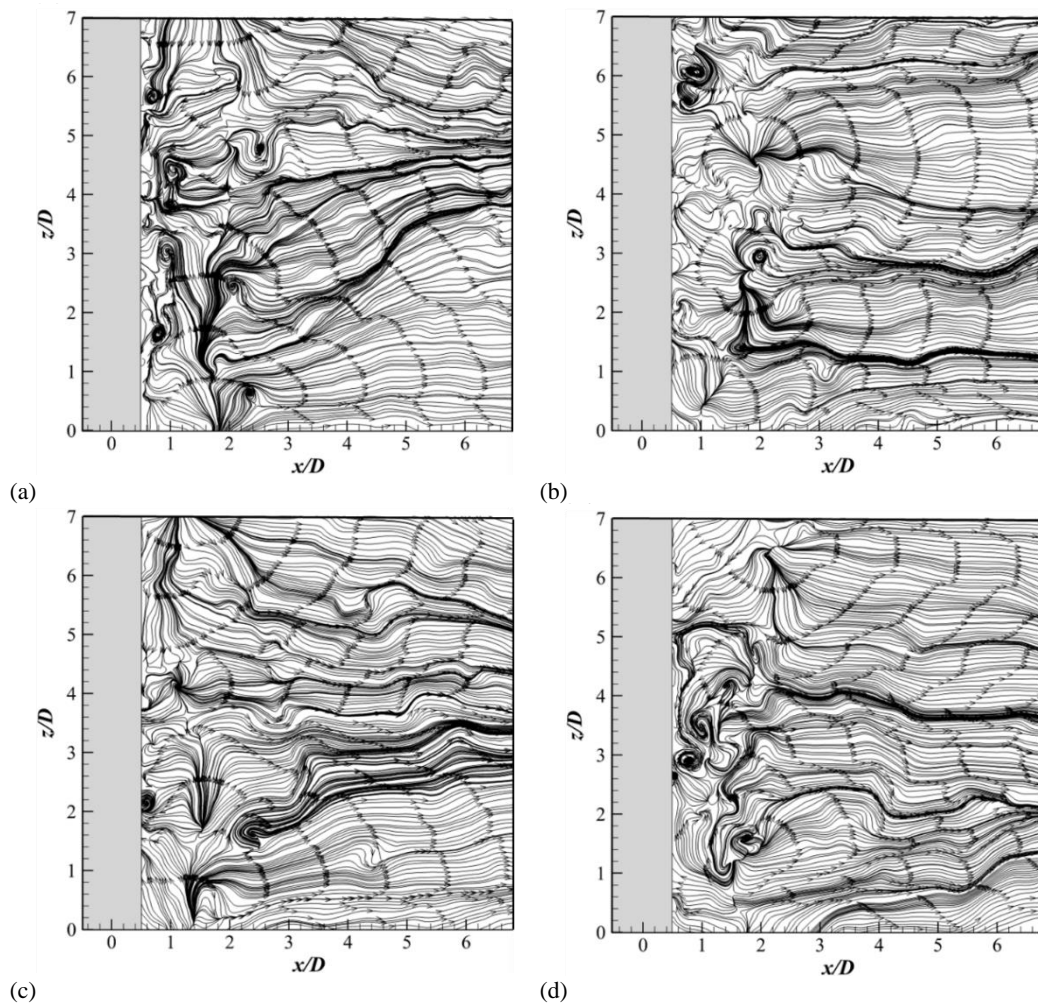


Fig. 17. Instantaneous streamlines in the (x, z) -plane of $y=0$. (a) smooth cylinder, (b) secondary grooved cylinder with $h/D=0.035$, (c) secondary grooved cylinder with $h/D=0.05$, (d) secondary grooved cylinder with $h/D=0.1$.

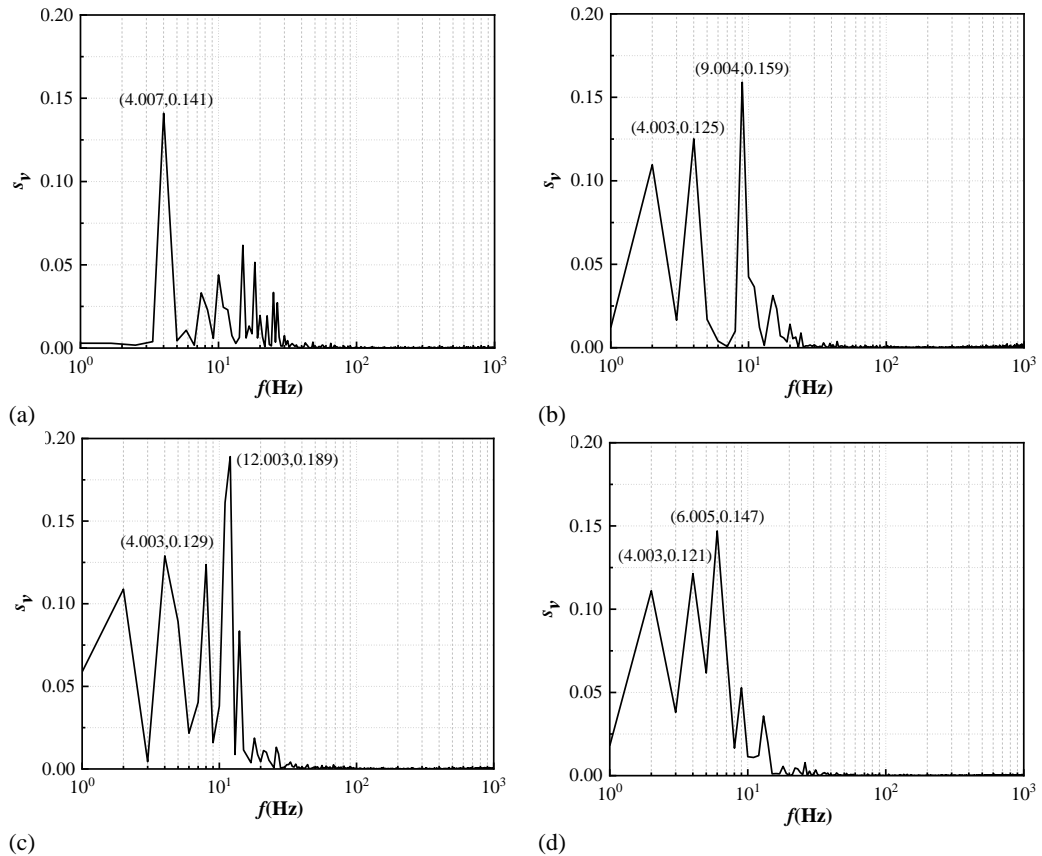


Fig. 18. Spectral S_v of velocity component v at $x/D = -1.2$, $y/D = 0.3$ and $z = 0$. (a) smooth cylinder, (b) secondary grooved cylinder with $k/D=0.035$, (c) secondary grooved cylinder with $k/D=0.05$, (d) secondary grooved cylinder with $k/D=0.1$.

For secondary grooved cylinders with different depths, the presence of multiple peaks can be observed, as shown in Fig. 18(b), with the two peaks corresponding to the frequencies $f = 4.003$ ($St = 0.21$) and $f = 9.004$ ($St = 0.47$) being the most significant. The phenomenon of multiple peaks is also present in Fig. 18(c) and (d). This may be because the secondary groove structure inhibits the length of vortex formation in the wake region, causing the velocity fluctuations to become unstable. Therefore, the multi-peak phenomenon is generated.

The frequency corresponding to the peak represents the frequency of vortex shedding, indicating that the secondary groove structure affects the frequency of vortex shedding. The multi-peak phenomenon indicates that small-scale vortices coexist with large-scale vortices and are in the same shedding state. At the same time, the increase of the peak indicates the increase of the turbulence intensity in the wake of the secondary grooved cylinders with different depths. In particular, the peak is largest for the secondary grooved cylinder with $h/D = 0.05$.

4. CONCLUSION

The wake structure of secondary grooved cylinders with different depths was experimentally investigated in this study using particle image velocimetry (PIV), which was used to examine time-

averaged streamlines, time-averaged velocity, RMS velocity, Reynolds stress, turbulent kinetic energy, instantaneous flow structures and spectral characters. The following conclusions can be drawn.

- (1) The length of the recirculation zone was reduced by the secondary groove structure, especially for the secondary grooved cylinder with $h/D=0.05$. At the same profile position, the velocity gradient of secondary grooved cylinders with different depths at each position is smaller compared to the smooth cylinder, especially for the secondary grooved cylinder with $h/D=0.05$.
- (2) The secondary groove structure reduces the magnitude of the peak of the fluctuation intensity of the flow velocity and lateral velocity and delays the location of the peak, which is most obvious in the secondary grooved cylinder with $h/D=0.05$.
- (3) The flow structure in the cylinder's wake region is affected by or altered by the secondary groove structure, where the tip structure also plays an important role in increasing the turbulent fluctuations in the boundary layer, especially in the secondary grooved cylinder with $h/D=0.05$, where the maximum Reynolds stress value is increased by 64.3%, and the maximum value of

turbulent kinetic energy is increased by 35.7%.

- (4) The transient large-scale vortex is split into several smaller scale vortices behind the secondary grooved cylinders, especially in the secondary grooved cylinder with $h/D=0.05$.
- (5) For the spectral characteristics of the velocity component, the frequency of vortex shedding increases for secondary grooved cylinders with different depths, and the phenomenon of multiple peaks appears, especially in the secondary grooved cylinder with $h/D = 0.05$.

ACKNOWLEDGEMENTS

The author wishes to acknowledge the support given to him by the Natural Science Foundation of Jiangsu Province of China (No. BK20191459), Postgraduate Research & Practice Innovation Program of Jiangsu Province of China (SJCX22_1928).

REFERENCES

- Afroz, F. and M. A. R. Sharif (2022). Numerical study of cross-flow around a circular cylinder with differently shaped span-wise surface grooves at low Reynolds number. *European Journal of Mechanics/B Fluids* 91, 203-218.
- Aguedal, L., D. Semmar, A. S. Berrouk, A. Azzi and H. Oualli (2018). 3D vortex structure investigation using Large Eddy Simulation of flow around a rotary oscillating circular cylinder. *European Journal of Mechanics/B Fluids* 71, 113-125.
- Assi, G. R. S., P. W. Bearman and M. A. Tognarelli (2014). On the stability of a free-to-rotate short-tail fairing and a splitter plate as suppressors of vortex-induced vibration. *Ocean Engineering* 92, 234-244.
- Baek, H. and G. E. Karniadakis (2009). Suppressing vortex-induced vibrations via passive means. *Fluids Struct* 25, 848-866.
- Canpolat, C. (2015). Characteristics offlow past a circular cylinder with a rectangular groove. *Flow Measurement and Instrumentation* 45, 233-246.
- Canpolat, C. (2017). Influence of single rectangular groove on the flow past a circular cylinder. *International Journal of Heat and Fluid Flow* 64, 79-88.
- Cao, Y. and T. Tamura (2015). Numerical investigations into effects of three-dimensional wake patterns on unsteady aerodynamic characteristics of a circular cylinder at $Re=1.3\times 10^5$. *Fluids Struct* 59, 351-369.
- Fujisawa, N., K. Hirabayashi and T. Yamagata (2020). Aerodynamic noise reduction of circular cylinder by longitudinal grooves. *Journal of Wind Engineering and Industrial Aerodynamics* 199, 104129.
- Gu, F., J. S. Wang, X. Q. Qiao and Z. Huang (2012). Pressure distribution, fluctuating forces and vortex shedding behavior of circular cylinder with rotatable splitter plates. *Fluids Struct* 28, 263-278.
- Huang, S. (2011). VIV suppression of a two-degree-of-freedom circular cylinder and drag reduction of a fixed circular cylinder by the use of helical grooves. *Journal of Fluids and Structures* 27, 1124-1133.
- Hwang, J. Y. and K. S. Yang (2007). Drag reduction on a circular cylinder using dual detached splitter plates. *Journal of Wind Engineering and Industrial Aerodynamics* 95, 551-564.
- Law, Y. Z. and R. K. Jaiman (2018). Passive control of vortex-induced vibration by spanwise grooves. *Fluids Struct* 83, 1-26.
- Lim, H. C. and S. J. Lee (2003). PIV measurements of near wake behind a U-grooved cylinder. *Fluids Struct* 18, 119-130.
- Liu, K., J. Deng and M. Mei (2016). Experimental study on the confined flow over a circular cylinder with a splitter plate. *Flow Measurement and Instrumentation* 51, 95-104.
- Liu, Y. Z., L. L. Shi and J. Yu (2011). TR-PIV measurement of the wake behind a grooved cylinder at low Reynolds number. *Fluids Struct* 27, 394-407.
- Liu, Z. Y., H. B. Hu and B. W. Song (2009). Numerical Simulation Research about Riblet Surface with Different Spacing. *Journal of System Simulation* 19, 6025-6032.
- Oeffner, J. and G. V. Lauder (2012). The hydrodynamic function of shark skin and two biomimetic applications. *Journal of Experimental Biology* 215, 785-795.
- Qian, Q. and G. R. Wang (2019). Numerical simulation of drag reduction of V-grooved circular cylinder at subcritical Reynolds number. *Advances in Marine Science* 37(1), 150-160.
- Quintavalla, S. J., A. J. Angilell and A. J. Smits (2013). Drag reduction on grooved cylinders in the critical Reynolds number regime. *Experimental Thermal and Fluid Science* 48, 15-18.
- Rinoshika, H. and A. Rinoshika (2018). Effect of a horizontal hole on flow structures around a wall-mounted low-aspect-ratio cylinder. *International Journal of Heat and Fluid Flow* 71, 80-94.
- Rinoshika, H. and A. Rinoshika (2019). Passive control of a front inclined hole on flow structures around a surface-mounted short cylinder. *Ocean Engineering* 189, 106383.
- Sumner, D. (2009). Temporal Development of the

- Wake of a Non-Impulsively Started Circular Cylinder. *Fedsm* 78018, 1-8.
- Takayama, S. and K. Aoki (2005). Numerical analysis of flow characteristics around circular cylinders with arc grooves (school of engineering). *Proceedings of the School of Engineering of Tokai University* 30, 1-5.
- Talley, B. S. and G. Mungal (2002). Flow around cactus-shaped cylinders. Center for Turbulence Research Annual Research Briefs 2002, 363-376.
- Wang, G. R., C. J. Liao and G. Hu (2017). Numerical simulation analysis and the drag reduction performance investigation on circular cylinder with dimples at subcritical Reynolds number. *Journal of Mechanical Strength* 39(05), 1119-1125.
- Xie, F. F., Y. Yue and G. E. Karniadakis (2015). U-shaped fairings suppress vortex-induced vibrations for cylinders in cross-flow. *Fluid Mech* 782, 300-332.
- Xu, C. Y., L. W. Chen and X. Y. Lu (2010). Large-eddy simulation of the compressible flow past a wavy cylinder. *Fluid Mech* 665, 238-273.
- Zheng, C. T., P. Zhou and S. Y. Zhong (2021). An experimental investigation of drag and noise reduction from a circular cylinder using longitudinal grooves. *Physics of Fluids* 33, 115110.
- Zheng, Y. and H. Rinoschik. (2020). Analyses on flow structures behind a wavy square cylinder based on continuous wavelet transform and dynamic mode decomposition. *Ocean Engineerin.* 216, 108-117.
- Zhou, T., S. F. M. Razali and Z. Hao (2011). On the study of vortex-induced vibration of a cylinder with helical strakes. *Fluids Struc* 27, 903-917.
- Zhou, B., X. Wang, W. Guo, W. M. Gho and S. K. Tan (2015a). Experimental study on flow past a circular cylinder with rough surface. *Ocean Engineering* 109, 7-13.
- Zhou, B., X. K. Wang and W. Guo (2015b). Control of flow past a dimpled circular cylinder. *Experimental Thermal and Fluid Science* 69, 19-26.
- Zhou, B., X. K. Wang and W. Guo (2015c). Experimental measurements of the drag force and the near-wake flow patterns of a longitudinally grooved cylinder. *Journal of Wind Engineering and Industrial Aerodynamic* 145, 30-41.
- Zhu, H. J. (2017). *Suppression Method of Vortex Induced Vibration of Marine Risers*. Petroleum Industry Press.
- Zhu, H. J. and T. M. Zhou (2019). Flow around a circular cylinder attached with a pair of fin-shaped strips. *Ocean Engineering* 190, 106484.